The apparent mechanical effect of isolated amyloid-β and α-synuclein aggregates revealed by multi-frequency MRE

Mathilde Bigot, Fabien Chauveau, Camille Amaz, Ralph Sinkus, Olivier Beuf, Simon A. Lambert

The apparent mechanical effect of isolated Aβ and α-Syn aggregates revealed by multi-frequency MRE

Mathilde Bigot[1], Fabien Chauveau[2], Camille Amaz[3], Ralph Sinkus[4], Olivier Beuf[1], Simon A. Lambert[1]

[1]Université de Lyon, INSA-Lyon, Université Claude Bernard Lyon 1, UJM-Saint Etienne, CNRS, Inserm, CREATIS UMR 5220, U1206, F69621, Lyon, France, [2]Lyon Neuroscience Research Center, UMR5292, Institut national de la Santé et de la Recherche Médicale, Université Lyon 1, Lyon, France, [3]Service des explorations fonctionnelles cardiovasculaires, Louis Pradel Hospital, Hospices Civils de Lyon, 28 avenue Doyen Lépine, 69677 BRON Cedex, France, [4]INSERM U 1148, Laboratory of Vascular Translational Science; X. Bichat Hospital University Paris Diderot, Paris, France,

Number of words (body of text): 3,091

Running title: Effect of Aβ and α-Syn aggregates revealed by multi-frequency MRE

Keywords (8): MR Elastography, fibril aggregates, amyloid, phantom, multi-frequency, power law exponent, dementia, fractal-like

Correspondence to:

Simon A. Lambert, Université de Lyon, INSA-Lyon, Université Claude Bernard Lyon 1, UJM-Saint Etienne, CNRS, Inserm, CREATIS UMR 5220, U1206, F69621, Lyon, France

E-mail: Simon.Lambert@creatis.insa-lyon.fr

Abstract

Several biological processes are involved in dementia, and fibrillar aggregation of misshaped endogenous proteins appears to be an early hallmark of neurodegenerative disease. A recently developed means of studying neurodegenerative diseases is Magnetic Resonance Elastography (MRE), an imaging technique investigating the mechanical properties of tissues. Although mechanical changes associated with these diseases have been detected, the specific signal of fibrils has not yet been isolated in clinical or pre-clinical studies. The present study aims to exploit the fractal-like properties of fibrils to separate them from non-aggregated proteins using a multi-frequency MRE power law exponent in a phantom study.

Two types of fibril, α-Syn and Aβ, and a non-aggregated protein, Bovine Serum Albumin, used as control were incorporated in a dedicated non-dispersive agarose phantom. Elastography was performed at multiple frequencies between 400 and 1,200 Hz. After 3D-direct inversion, storage modulus G', phase angle φ, wave speed c and the power law exponent y were computed.

No significant changes in G' and φ were detected. Both α-Syn and Aβ inclusions showed significantly higher y values than control inclusions ($p = 0.005$) but did not differ between each other.

The present phantom study highlighted a specific biomechanical effect of α-Syn and Aβ aggregates which was better captured with the power law exponent derived from multi-frequency MRE than with single frequency derived parameters.

Graphical abstract

The apparent mechanical effect of isolated Aβ and α-Syn aggregates revealed by multi-frequency MRE

M. Bigot, F. Chauveau, R. Sinkus, O. Beuf, S. A. Lambert

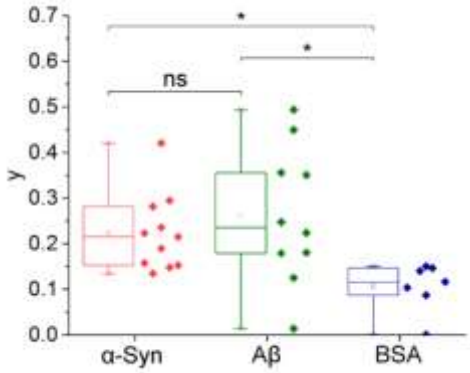

Multi-frequency MR Elastography was used on agarose phantoms with small inclusions containing protein aggregates, early hallmarks of dementias. α-Syn and Aβ, the two types of studied aggregates had significantly high power law exponent compared with a non-aggregated protein used as control, while MRE parameters at a single frequency did not discriminate those aggregates from control. Their fractal-like structure based on β-sheets might be the source of their effect on power law exponent.

Abbreviations used

- α-Syn, α-synuclein
- Aβ, amyloid β
- φ, phase angle
- AD, Alzheimer's Disease
- BSA, Bovine Serum Albumin
- c, wave speed
- f, frequency
- k, complex wave number
- k_r, real part of the complex wave number
- G', storage modulus
- G", loss modulus
- G*, complex shear modulus;
- MEG, Motion Encoding Gradient
- MSME, Multi-Slice Multi-Echo
- MRE, Magnetic Resonance Elastography
- PBS, Phosphate Buffer Saline
- PET-CT, Positron Emission Tomography – Computed Tomography
- ROI, Region Of Interest
- y, power-law exponent

Introduction

Dementias are neurodegenerative diseases characterized by a decline in mental ability. Progression involves several biological processes such as impaired neurotransmission, inflammation, neurodegeneration and, from the early stages, fibrillar aggregation of misshaped endogenous proteins[1–3]. These fibrils appear to be hallmarks of dementia: in the wide span of neurodegenerative diseases, distinct endogenous proteins, such as amyloid-β, α-synuclein or Tau, share a common mechanism of pathological aggregation and spreading across brain areas[4]. They also share a microstructural feature: all misshape to form β-sheets.

A recent means of studying neurodegenerative diseases is Magnetic Resonance Elastography (MRE), an imaging technique investigating mechanical properties of tissues[5]. The most popular MRE method uses a monochromatic shear wave propagated through tissue and synchronized with oscillating motion encoding gradients (MEG). The wave fields acquired are typically processed using a viscoelastic wave equation, leading to mechanical property maps: i.e., information on elasticity and viscosity.

MRE has been used in both preclinical and clinical studies on dementia. Recent clinical studies showed that brain stiffness varied between areas according to pathology[6]. Stiffness was decreased in frontal and temporal lobes in frontotemporal dementia[7], lentiform nucleus in Parkinson's disease[8], and frontal, temporal and parietal lobes in Alzheimer's disease (AD)[9]. Small-animal studies confirmed decreased stiffness and further suggested an association with neuronal loss[10–15]. A biomechanical study in a multiple sclerosis mouse model showed that phase angle was sensitive to demyelination and remyelination[16].

Few studies have specifically focused on the influence of AD amyloid β (Aβ) fibrils on MRE parameters. In humans, a study comparing AD patients testing positive versus negative for presence of Aβ according on PET-CT suggested that amyloid load alone could not explain the changes in stiffness observed[17]. In a mouse model of AD, increased storage modulus (representing elasticity) correlated with intracellular fibril load during adolescence, attributed to change in cell structure. However, in older mice, no link was found between extracellular presence of Aβ and viscoelastic parameters[13]. Overall, most studies suggested that protein aggregation might not be the main factor driving brain stiffness changes. However, concurrent pathological phenomena such as inflammation, neurodegeneration or vascular impairment cannot be easily disentangled in living organisms.

In the last decade, various teams reported that multi-frequency MRE could reveal the underlying microstructure of matter at a macroscopic scale. Whatever the mechanical model, the frequency-

dependence of the MRE-derived parameters could be fitted to a power law, and the exponent of this power law could be linked to the underlying microarchitecture. The exponent was reported to be reduced in chronic multiple sclerosis while remaining constant in relapsing-remitting multiple sclerosis. Altered cerebral structures in the chronic case were a possible explanation for this difference[18,19]. To establish the link between the power law exponent and the underlying microarchitecture, some studies used calibrated phantoms, made with a single type of microstructure such as paper strips[20], microvasculature[21] or polystyrene microsphere distribution[22]. In a polystyrene microsphere phantom, Lambert et al. used wave propagation to show that multiple wave scattering on microscopic rigid scatterers resulted macroscopically in power law frequency-dependence of wave speed. The exponent of the power law was linked to the apparent fractality of the medium. Importantly, for the geometrically induced power law to be established, the scattering objects need to be not too small compared to the shear wavelength; otherwise, apparent attenuation vanishes and only the material's constitutive dispersion matters.

Like microspheres and vessels, fibrils are more rigid than their surrounding glial cells[23,24] and can induce multiple scattering of propagating shear waves. Moreover, their repetitive β-sheet structure over a large scale (from protein diameter to a few mm) confers fractal-like properties. This fractality in the empirical data can be observed only over a limited range[25,26] as long as it is sufficiently large: i.e., according to Lazzari et al., the upper limit should be "20 times larger than the primary particle"[27]. We propose here to exploit these properties, using multi-frequency MRE to study the effect of two types of fibril on shear wave scattering in a non-dispersive agarose medium. This phantom study seeks to improve understanding of the specific contribution of protein fibrils to mechanical changes observed in the brain.

Methods

Sample preparation

Dedicated phantoms with well-delineated fibril inclusions were produced to isolate the effect of fibrils using a purely elastic agarose base. In this lossless environment, any frequency dependence of speed mainly originates from multiple scattering of waves due to the presence of obstacles, such as fibrils[22,28].

Fibrils of human recombinant proteins (rPeptide), amyloid-β peptide 1-40 (Aβ) and full-length A53T-mutated α-synuclein (α-Syn) were prepared as previously described[29,30]. Aggregation was controlled with thioflavin-T fluorimetry and transmission electron microscopy after uranyl-acetate staining.

Phantoms were made with 1 % agarose powder (Sigma A9414) diluted in artificial cerebrospinal fluid[31], to have composition and mechanical properties similar to the brain. In each phantom, a maximum of four 3 x 3 x 3 mm^3 inclusions were made, using a mold (Fig. 1). Each inclusion was filled as follows: 21% of one type of aggregated fibrils at high concentration in PBS solution (initial monomer concentration, 200 µM), 5% thioflavin-T solution (0.01% in PBS) for fluorescence imaging, and 74% agarose. Agarose mass concentration was 1.35% in the 4 inclusions, to compensate the effect of dilution on mechanical properties. One inclusion was used as control, containing Bovine Serum Albumin (BSA, Carl Roth, ref. 3737), a non-aggregated protein, at a mass concentration of 4.3 mg/mL in PBS. Red Congo staining was used to visually locate this control inclusion and hence facilitate phantom positioning on MRI (Fig. 1).

Altogether, 7 phantoms were produced, with 11 α-Syn inclusions, 10 Aβ inclusions and 7 BSA inclusions. Phantoms were directly molded in their holder and covered by paraffin wax (DTM 133460) to prevent dehydration and bulk motion during actuation.

Macrofluorescence

To check that fibrils did not migrate out of the inclusions, fluorescence microscopy (Leica Macrofluo Z16 APA A) was performed on the whole phantom after MRE imaging. Thioflavin-T, which binds to fibrils and emits green fluorescence, was used as fluorochrome (Fig. 2).

MRE set-up

Experimental set-up

The sample holder was slid inside a homemade 3D-printed Helmholtz coil (Fig. 3) designed to maximize uniformity and filling factor (Fig. S1) and to facilitate vertical handling of small samples.

The volume coil was simply taped to a dedicated elastography bench, so that a needle pierced the sample. The needle was fixed on a Plexiglas flap, linked to an air-cooled piezoelectric driver (APA100M Cedrat Technologies) via a star-shaped plastic rod. Actuator frequency and amplitude were set by a function generator (33220A Agilent Technologies) through an amplifier (LA75 Cedrat Technologies).

Data acquisition

All acquisitions were performed on a pre-clinical 4.7 T MRI scanner (BioSpec Bruker system, Ettlingen, Germany). The MRE sequence was derived from a RARE sequence[32], and was performed sequentially at 600-800-900-1,000-400-1,200-600 Hz. Acquisition at 600 Hz was performed at the beginning and repeated at the end of elastography to check that the sample's mechanical properties did not alter over time (MRE

exam duration, 1h45). Sinusoidal Motion Encoding Gradients (MEG) with 180 $mT.m^{-1}$ amplitude were synchronized with the piezoelectric driver through a trigger sent by the MRI console. To establish steady-state regime before phase encoding, 40 wave periods were performed ahead of MEG. For each frequency, MRE acquisition was repeated 3 times, with change in MEG orientation (slice, phase, read) to acquire the 3 directions of motion. Number of MEG periods and echo time were adjusted according to frequency so as to maximize SNR (SNR varying between 23 at 400 Hz and 17 at 1,000 Hz). To minimize acquisition time, a RARE factor of 2 was used.

An MSME (multi-slice multi-echo) sequence was acquired to locate inclusions on the computed T2-maps and facilitate ROI positioning, as explained below.

Further details on both MRE and MSME sequences are given in Table 1.

Post-processing

Data processing was performed as described by Sinkus et al.[33]. Raw phase images were unwrapped, filtered with a 3D-Gaussian filter (kernel = 2 x 2 x 2, σ = 0.39 x 0.39 x 1 mm^3) and Fourier transformed into 3D displacement fields. 3D curl inversion was applied to the fields to calculate the complex shear modulus G* and the complex wave number k at each acquired frequency.

Image analysis

ROIs were manually drawn only on the central slice, excluding inclusion borders, to avoid bias due to reconstruction artifacts or slice positioning error (Fig. 2b). In-plane, inclusions were located on T2-maps and reported on MRE acquisitions. Only central inclusion areas were included, to avoid inhomogeneity at the corners of the inclusions and edge reconstruction effects, leading to ROI sizes ranging between 10 and 38 pixels. One ROI close in size was also drawn in simple agarose for each sample.

The mean and standard deviation of the real and imaginary parts of G* (storage modulus G' standing for elasticity and loss modulus G" standing for viscosity) and real part of k (k_r) inside the ROIs were computed. Mean phase angle $\varphi = tan^{-1}\left(\frac{G"}{G'}\right)$ and wave speed $c = \frac{2\pi f}{k_r}$ were derived. The relation between wave speed c and excitation frequency f was fitted on a power law: $c = af^y$. Unwrapped phase and wave speed at 400 and 1,200 Hz are shown as an example Figure 4. φ and y are two variables shown to be related to underlying microstructure in previous studies. The relation φ = πy can be deduced from literature, but is only valid when φ is independent of frequency[34–36].

Statistics

All results are reported as mean ± standard deviations. Statistical tests used OriginPro 2016 and R statistical software version 3.3.3. Only the first of the two 600 Hz acquisitions was taken into account, so as to have the same number of data points as for the other frequencies. The significance threshold α was set at 0.05/3 = 0.017 to correct for multiple comparisons between the three groups (Aβ, α-Syn, BSA).

First, differences in the microstructure-sensitive parameter y were assessed on non-parametric analysis of variance (Kruskal-Wallis test), followed by Kolmogorov-Smirnov tests.

Second, G', Phi, c were evaluated by using linear mixed-effects models that included groups (α-Syn, Aβ, BSA) and frequency as fixed-effect and random effect grouped by phantom used. Results are reported as effect size β, confidence interval CI, and p-value. For relevant parameters identified by the linear mixed model, exploratory comparisons were also performed at each frequency to simulate the fastest and most commonly performed single-frequency acquisitions.

Finally, to confirm the validity of the mathematical relation between φ and y, an additional Kruskal-Wallis test was performed to evaluate the frequency dependence of φ.

Results

Macrofluorescence results

Macrofluorescence revealed no fibril leakage out of the inclusion areas (Fig. 2b). However, the fluorescence distribution was non-homogeneous for some inclusions.

Differences in elastic properties between fibrils and BSA

Mean relative difference in k_r measured in inclusions between the first and last 600-Hz acquisitions was 3±2%. A homogeneous 1% agarose phantom without inclusion was also characterized at 600 Hz over a 23-hour period (15 measures) to demonstrate the mechanical stability of agarose over time: the standard deviation of k_r was only 1% of the mean value.

Linear mixed-effects models showed no group effect on wave speed c (Fig. 5a), or on storage modulus (Fig. 5b), even though G' and c tend to be smaller in the fibril groups at low frequency. Datasets and results of linear mixed-effects models are provided as supplemental Excel file.[MB1]

Difference in structural parameters y and φ between fibrils and BSA

Both α-Syn and Aβ inclusions showed significantly higher values of exponent y than BSA inclusions ($y_{\alpha\text{-Syn}}$ = 0.22±0.08; $y_{A\beta}$ = 0.26±0.15; y_{BSA} = 0.11±0.05 – p = 0.005, Fig. 6a), but did not differ between each other. Of note, no difference was observed between BSA inclusions and simple agarose outside the inclusions (p = 0.963; complete results extracted from agarose ROIs outside the inclusions are reported in Supplementary Table S2).

Parameter φ was not significantly different between both fibril groups and BSA. A trend toward higher values in fibril groups is however noticeable (Fig. 6b). [MB2]Frequency had an impact on φ distribution (Kruskal-Wallis test on pooled values from all frequencies, p < 0.0003).

Discussion

Detection of a fibril-specific effect

Fibrils are macromolecular protein assemblies of β-sheet stacks and are considered to be an early hallmark of neurodegenerative diseases[1–3]. Their specific effect on MRE parameters could not easily be inferred from previous studies of transgenic mice and patients[13,17]. In the present, we simplified the fibril environment to isolate a potential effect on various MRE-derived parameters. More specifically, we used their fractal-like distribution[27] as a source of multiple scattering of shear waves that leaves its footprint in the exponent of the frequency power law. Surprisingly, MRI becomes sensitive to nanometric structures because of the spatial extent induced by apparent fractality. Based upon stiffness itself, fibrils are difficult to distinguish: no difference was found between the two fibril groups versus BSA using single-frequency MRE parameters. Therefore y is really an added value to characterize the underlying microarchitecture: e.g., here for fibril detection.

BSA, a non-aggregated protein, did not modify the dispersion properties of agarose, while the two fibril types were able to significantly increase the power law exponent y, confirming that fibrils are a dispersive obstacle for shear waves. Aβ and α-Syn are made of different proteins, and their aggregation leads to fibrils harboring different widths and lengths, as visible on transmission electron microscopy images (provided as Supplementary Figure S3). No significant difference in y was found between the two types of fibril, suggesting that their common architectural base, β-sheet stacks, behaves as a fractal-like object, leading to the same frequency-dependence of mechanical properties.

Based on our results, predicting a potential overruling of fibril effect by other modifications in the case of neurodegenerative diseases remains delicate, since the sensitivity of detection in this study was difficult to estimate: firstly because the exact concentration of fibrils was unknown (monomer concentration was 200 µM, but the number of monomers per fibril unit could not be easily estimated), and secondly because of fluorescence inhomogeneities, probably deriving from the difficulty of mixing fibrils with agarose. Such a multi-frequency MRE experiment could be used on *ex vivo* and *in vivo* brain to screen for an effect of fibrils on mechanical properties. However, demonstrating a specific effect of fibrils among all the other microstructural changes involved in neurodegenerative disease and in *in vivo* conditions might require full brain characterization at the microscopic scale using quantitative and 3D histological methods (neuronal loss, glial activation, etc.)[37].

Relevance of multi-frequency study

Multi-frequency MRE allowed an effect of isolated fibrils on mechanical parameters to be shown for the first time. The power law exponent was significantly altered by fibril presence, unlike the storage modulus, wave speed and phase angle.

A tendency for G' to be smaller in the fibril groups at low frequency was noted. We think that this observation cannot be explained by a change in microstructure, and rather arise from an interference with the agarose polymerization process.[MB3] In addition, the changes in wave speed and elasticity appear to be very similar on graphs, possibly because of similar absorption (i.e. imaginary part of k) in both BSA and fibrils[38]. The absence of a fibril effect at high frequencies on viscoelasticity parameters corroborates preclinical[13] and human[17] findings.

Like the power law exponent, φ globally increased, however non significantly, in the presence of fibrils. Since both parameters were reported to provide information on microstructure[16,21], this similarity was expected. Some limitations in the use of φ have to be pointed out: the dependence of φ on G'' value was problematic, since the phantoms were almost elastic: i.e., G'' was small compared to G'. φ values might thus have been affected by noise. As underlined by Dittman et al., φ estimation is not robust to noise, worsening this effect[39]. This explains why the difference between fibrils and BSA was not significant when φ was considered only at a given frequency.

Another aspect ruling out φ as a reliable dispersion parameter is the frequency-dependence demonstrated here, which makes φ mathematically unrelated to y[36]. As expected, the data exhibited a frequency power law, expressed by y, which stems from a fit of the wave speed to the six frequencies. If data additionally

followed the rheological model of a spring pot, slope y could be calculated from phase angle at each individual frequency. Our data do not support this hypothesis, as shown by the fact that φ did not show the same separation for different material constructs as y. A theoretical model matching this observation is when both the temporal and the spatial operator in equation $\varphi = tan^{-1}\left(\frac{G"}{G'}\right)$ are of fractional order. This yields one parameter modifying the slope of the frequency behavior and an additional parameter impacting the ratio of G'' to G'[40].

It seems difficult to dispense with multi-frequency MRE and to extract the power law parameter for fibril characterization. However, multi-frequency MRE is long to perform, *ex* or *in vivo*. It could benefit from sequences with reduced acquisition time[41–43]. We used six frequencies with a rather large range to enhance fitting quality, but the number of acquisitions could be reduced according to Clauset et al., since the power law model is well established[44].

Perspectives for preclinical follow-up

In this study performed on phantoms, the presence of fibrils was the only factor affecting y. Under *in vivo* conditions, additional tissue complexity could mask the fibril effect that we measured in a simple phantom, and neurodegenerative diseases moreover involve several additional microscopic changes in brain. Microstructural changes such as demyelination[16] or age-related decrease in neuron density[45] have also been shown to induce mechanical changes. Such variability makes the relationship between MRE measurements and biological processes even more difficult to elucidate. In the case of chronic multiple sclerosis, the specific structure triggering a modification of power law exponent is still unclear. Similarly, it is difficult to link phase angle variations to a specific physiological or pathological change in the brain: φ was found unchanged by an increase in cerebral blood flow[46], and decrease in neuron number[47] and inflammation[48], while changes in φ were reported in rodents for demyelination[16] and in the hippocampal area of AD patients, regardless of amyloid status[49]. φ also correlated with memory performance in healthy volunteers in the hippocampal area[50]. Finally, the heterogeneity of the structural composition in the brain may make the fibril effect on y or φ brain-area dependent.

Conclusion

In conclusion, the power law exponent derived from multi-frequency MRE data showed significant changes due to the presence of α-Syn and Aβ aggregates immersed in a homogeneous non-viscous medium. This phantom study isolated a specific effect of fibrils, independently of other changes associated with their accumulation in the brain.

Acknowledgments

This work was supported by the LABEX PRIMES (ANR-11-LABX-0063) of Université de Lyon, (France), within the *Programme Investissements d'Avenir* (ANR-11-IDEX-0007) and CNRS PEPS Balanced. It benefited from experimental expertise acquired on the PILoT platform, a member of the France Life Imaging network (ANR-11-INBS-0006) and on the LYMIC - PLATIM platform. We thank the RHU MARVELOUS (ANR-16-RHUS-0009) for providing a framework where statistical analysis was performed. We also thank Kevin Tse Ve Koon and Pauline Lefebvre for MRE sequence implementation and fruitful discussions.

References

1. Seelaar H, Rohrer JD, Pijnenburg YAL, Fox NC, Swieten JC van. Clinical, genetic and pathological heterogeneity of frontotemporal dementia: a review. *Journal of Neurology, Neurosurgery & Psychiatry*. January 2010:jnnp.2010.212225. doi:10.1136/jnnp.2010.212225.

2. Braak H, Tredici KD, Rüb U, de Vos RAI, Jansen Steur ENH, Braak E. Staging of brain pathology related to sporadic Parkinson's disease. *Neurobiology of Aging*. 2003;24(2):197-211. doi:10.1016/S0197-4580(02)00065-9.

3. Nelson PT, Alafuzoff I, Bigio EH, Bouras C, Braak H, Cairns NJ, Castellani RJ, Crain BJ, Davies P, Del Tredici K, Duyckaerts C, Frosch MP, Haroutunian V, Hof PR, Hulette CM, Hyman BT, Iwatsubo T, Jellinger KA, Jicha GA, Kövari E, Kukull WA, Leverenz JB, Love S, Mackenzie IR, Mann DM, Masliah E, McKee AC, Montine TJ, Morris JC, Schneider JA, Sonnen JA, Thal DR, Trojanowski JQ, Troncoso JC, Wisniewski T, Woltjer RL, Beach TG. Correlation of Alzheimer Disease Neuropathologic Changes With Cognitive Status: A Review of the Literature. *J Neuropathol Exp Neurol*. 2012;71(5):362-381. doi:10.1097/NEN.0b013e31825018f7.

4. Jucker M, Walker LC. Self-propagation of pathogenic protein aggregates in neurodegenerative diseases. *Nature*. 2013;501(7465):45-51. doi:10.1038/nature12481.

5. Muthupillai R, Lomas DJ, Rossman PJ, Greenleaf JF, Manduca A, Ehman RL. Magnetic resonance elastography by direct visualization of propagating acoustic strain waves. *Science*. 1995;269(5232):1854-1857.

6. ElSheikh M, Arani A, Perry A, Boeve BF, Meyer FB, Savica R, Ehman RL, Huston J. MR Elastography Demonstrates Unique Regional Brain Stiffness Patterns in Dementias. *AJR Am J Roentgenol*. 2017;209(2):403-408. doi:10.2214/AJR.16.17455.

7. Huston J, Murphy MC, Boeve BF, Fattahi N, Arani A, Glaser KJ, Manduca A, Jones DT, Ehman RL. Magnetic resonance elastography of frontotemporal dementia. *J Magn Reson Imaging*. 2016;43(2):474-478. doi:10.1002/jmri.24977.

8. Lipp A, Trbojevic R, Paul F, Fehlner A, Hirsch S, Scheel M, Noack C, Braun J, Sack I. Cerebral magnetic resonance elastography in supranuclear palsy and idiopathic Parkinson's disease. *NeuroImage: Clinical*. 2013;3:381-387. doi:10.1016/j.nicl.2013.09.006.

9. Murphy MC, Jones DT, Jack Jr. CR, Glaser KJ, Senjem ML, Manduca A, Felmlee JP, Carter RE, Ehman RL, Huston III J. Regional brain stiffness changes across the Alzheimer's disease spectrum. *NeuroImage: Clinical*. 2016;10:283-290. doi:10.1016/j.nicl.2015.12.007.

10. Majumdar S, Klatt D. In vivo cerebral MR elastography in a mouse model of Alzheimer's disease: preliminary results. In: Proceedings of the 25th Annual Meeting ISMRM. Honolulu, HI. 2017. p. 242

11. Klein C, Hain EG, Braun J, Riek K, Mueller S, Steiner B, Sack I. Enhanced Adult Neurogenesis Increases Brain Stiffness: In Vivo Magnetic Resonance Elastography in a Mouse Model of Dopamine Depletion. *PLOS ONE*. 2014;9(3):e92582. doi:10.1371/journal.pone.0092582.

12. Hain EG, Klein C, Munder T, Braun J, Riek K, Mueller S, Sack I, Steiner B. Dopaminergic Neurodegeneration in the Mouse Is Associated with Decrease of Viscoelasticity of Substantia Nigra Tissue. *PLOS ONE*. 2016;11(8):e0161179. doi:10.1371/journal.pone.0161179.

13. Munder T, Pfeffer A, Schreyer S, Guo J, Braun J, Sack I, Steiner B, Klein C. MR elastography detection of early viscoelastic response of the murine hippocampus to amyloid β accumulation and neuronal cell loss due to Alzheimer's disease. *J Magn Reson Imaging*. 2018;47:234-245. doi:10.1002/jmri.25741.

14. Murphy MC, Curran GL, Glaser KJ, Rossman PJ, Huston J, Poduslo JF, Jack CR, Felmlee JP, Ehman RL. Magnetic resonance elastography of the brain in a mouse model of Alzheimer's disease: initial results. *Magn Reson Imaging*. 2012;30(4):535-539. doi:10.1016/j.mri.2011.12.019.

15. Bigot M, Chauveau F, Beuf O, Lambert SA. Magnetic Resonance Elastography of Rodent Brain. *Front Neurol*. 2018;9. doi:10.3389/fneur.2018.01010.

16. Schregel K, Wuerfel E, Garteiser P, Gemeinhardt I, Prozorovski T, Aktas O, Merz H, Petersen D, Wuerfel J, Sinkus R. Demyelination reduces brain parenchymal stiffness quantified in vivo by magnetic resonance elastography. *Proc Natl Acad Sci USA*. 2012;109(17):6650-6655. doi:10.1073/pnas.1200151109.

17. Murphy MC, Huston J, Jack CR, Glaser KJ, Manduca A, Felmlee JP, Ehman RL. Decreased Brain Stiffness in Alzheimer's Disease Determined by Magnetic Resonance Elastography. *J Magn Reson Imaging*. 2011;34(3):494-498. doi:10.1002/jmri.22707.

18. Wuerfel J, Paul F, Beierbach B, Hamhaber U, Klatt D, Papazoglou S, Zipp F, Martus P, Braun J, Sack I. MR-elastography reveals degradation of tissue integrity in multiple sclerosis. *NeuroImage*. 2010;49(3):2520-2525. doi:10.1016/j.neuroimage.2009.06.018.

19. Streitberger K-J, Sack I, Krefting D, Pfüller C, Braun J, Paul F, Wuerfel J. Brain viscoelasticity alteration in chronic-progressive multiple sclerosis. *PLoS ONE*. 2012;7(1):e29888. doi:10.1371/journal.pone.0029888.

20. Guo J, Posnansky O, Hirsch S, Scheel M, Taupitz M, Braun J, Sack I. Fractal network dimension and viscoelastic powerlaw behavior: II. An experimental study of structure-mimicking phantoms by magnetic resonance elastography. *Phys Med Biol*. 2012;57(12):4041. doi:10.1088/0031-9155/57/12/4041.

21. Jugé L, Petiet A, Lambert SA, Nicole P, Chatelin S, Vilgrain V, Van Beers BE, Bilston LE, Sinkus R. Microvasculature alters the dispersion properties of shear waves--a multi-frequency MR elastography study. *NMR Biomed*. 2015;28(12):1763-1771. doi:10.1002/nbm.3438.

22. Lambert SA, Näsholm SP, Nordsletten D, Michler C, Juge L, Serfaty J-M, Bilston L, Guzina B, Holm S, Sinkus R. Bridging Three Orders of Magnitude: Multiple Scattered Waves Sense Fractal Microscopic Structures via Dispersion. *Phys Rev Lett*. 2015;115(9):094301. doi:10.1103/PhysRevLett.115.094301.

23. Smith JF, Knowles TPJ, Dobson CM, MacPhee CE, Welland ME. Characterization of the nanoscale properties of individual amyloid fibrils. *PNAS*. 2006;103(43):15806-15811. doi:10.1073/pnas.0604035103.

24. Lu Y-B, Franze K, Seifert G, Steinhäuser C, Kirchhoff F, Wolburg H, Guck J, Janmey P, Wei E-Q, Käs J, Reichenbach A. Viscoelastic properties of individual glial cells and neurons in the CNS. *PNAS*. 2006;103(47):17759-17764. doi:10.1073/pnas.0606150103.

25. Hamburger D, Biham O, Avnir D. Apparent fractality emerging from models of random distributions. *Phys Rev E*. 1996;53(4):3342-3358. doi:10.1103/PhysRevE.53.3342.

26. Ciccotti M, Mulargia F. Pernicious effect of physical cutoffs in fractal analysis. *Phys Rev E*. 2002;65(3):037201. doi:10.1103/PhysRevE.65.037201.

27. Lazzari S, Nicoud L, Jaquet B, Lattuada M, Morbidelli M. Fractal-like structures in colloid science. *Advances in Colloid and Interface Science*. 2016;235:1-13. doi:10.1016/j.cis.2016.05.002.

28. Yamakoshi Y, Sato J, Sato T. Ultrasonic imaging of internal vibration of soft tissue under forced vibration. *IEEE Transactions on Ultrasonics, Ferroelectrics, and Frequency Control*. 1990;37(2):45-53. doi:10.1109/58.46969.

29. Verdurand M, Chauveau F, Daoust A, Morel A-L, Bonnefoi F, Liger F, Bérod A, Zimmer L. Differential effects of amyloid-beta 1–40 and 1–42 fibrils on 5-HT1A serotonin receptors in rat brain. *Neurobiology of Aging*. 2016;40:11-21. doi:10.1016/j.neurobiolaging.2015.12.008.

30. Verdurand M, Levigoureux E, Zeinyeh W, Berthier L, Mendjel-Herda M, Cadarossanesaib F, Bouillot C, Iecker T, Terreux R, Lancelot S, Chauveau F, Billard T, Zimmer L. In Silico, in Vitro, and in Vivo Evaluation of New Candidates for α-Synuclein PET Imaging. *Mol Pharmaceutics*. 2018;15(8):3153-3166. doi:10.1021/acs.molpharmaceut.8b00229.

31. Alzet®. Preparation of Artificial CSF. alzet.com. http://www.alzet.com/products/guide_to_use/cfs_preparation.html. Published November 4, 2018. Accessed November 7, 2018.

32. Van Reeth E, Lefebvre PM, Ratiney H, Lambert SA, Tesch M, Brusseau E, Grenier D, Beuf O, Glaser SJ, Sugny D, Tse-Ve-Koon K. Constant gradient elastography with optimal control RF pulses. *Journal of Magnetic Resonance*. 2018;294:153-161. doi:10.1016/j.jmr.2018.07.013.

33. Sinkus R, Tanter M, Catheline S, Lorenzen J, Kuhl C, Sondermann E, Fink M. Imaging anisotropic and viscous properties of breast tissue by magnetic resonance-elastography. *Magn Reson Med*. 2005;53(2):372-387. doi:10.1002/mrm.20355.

34. Holm S, Sinkus R. A unifying fractional wave equation for compressional and shear waves. *The Journal of the Acoustical Society of America*. 2010;127(1):542-548. doi:10.1121/1.3268508.

35. Hirsch S, Braun J, Sack I. *Magnetic Resonance Elastography: Physical Background and Medical Applications*. Wiley-VCH; 2017. https://www.wiley.com/en-us/Magnetic+Resonance+Elastography%3A+Physical+Background+and+Medical+Applications-p-9783527340088. Accessed April 3, 2018.

36. Hiscox LV, Johnson CL, Barnhill E, McGarry MDJ, 3rd JH, Beek EJR van, Starr JM, Roberts N. Magnetic resonance elastography (MRE) of the human brain: technique, findings and clinical applications. *Phys Med Biol*. 2016;61(24):R401. doi:10.1088/0031-9155/61/24/R401.

37. Coelho S, Pozo JM, Costantini M, Highley JR, Mozumder M, Simpson JE, Ince PG, Frangi AF. Local volume fraction distributions of axons, astrocytes, and myelin in deep subcortical white matter. *NeuroImage*. 2018;179:275-287. doi:10.1016/j.neuroimage.2018.06.040.

38. Sinkus R, Lambert S, Abd-Elmoniem KZ, Morse C, Heller T, Guenthner C, Ghanem AM, Holm S, Gharib AM. Rheological determinants for simultaneous staging of hepatic fibrosis and inflammation in patients with chronic liver disease. *NMR in Biomedicine*. 2018;31(10):e3956. doi:10.1002/nbm.3956.

39. Dittmann F, Hirsch S, Tzschätzsch H, Guo J, Braun J, Sack I. In vivo wideband multifrequency MR elastography of the human brain and liver. *Magn Reson Med*. 2016;76(4):1116-1126. doi:10.1002/mrm.26006.

40. Valtorta D, Mazza E. Measurement of rheological properties of soft biological tissue with a novel torsional resonator device. *Rheol Acta*. 2006;45(5):677. doi:10.1007/s00397-005-0026-6.

41. Klatt D, Yasar TK, Royston TJ, Magin RL. Sample interval modulation for the simultaneous acquisition of displacement vector data in magnetic resonance elastography: theory and application. *Physics in medicine and biology*. 2013;58(24):8663. doi:10.1088/0031-9155/58/24/8663.

42. Kearney SP, Majumdar S, Royston TJ, Klatt D. Simultaneous 3D MR elastography of the in vivo mouse brain. *Phys Med Biol*. 2017. doi:10.1088/1361-6560/aa8444.

43. Guenthner C, Sethi S, Troelstra M, Dokumaci AS, Sinkus R, Kozerke S. Ristretto MRE: A generalized multi-shot GRE-MRE sequence. *NMR in Biomedicine*. January 2019. doi:10.1002/nbm.4049.

44. Clauset A, Shalizi C, Newman M. Power-Law Distributions in Empirical Data. *SIAM Rev*. 2009;51(4):661-703. doi:10.1137/070710111.

45. Sack I, Beierbach B, Wuerfel J, Klatt D, Hamhaber U, Papazoglou S, Martus P, Braun J. The impact of aging and gender on brain viscoelasticity. *NeuroImage*. 2009;46(3):652-657. doi:10.1016/j.neuroimage.2009.02.040.

46. Chatelin S, Humbert-Claude M, Garteiser P, Ricobaraza A, Vilgrain V, Van Beers BE, Sinkus R, Lenkei Z. Cannabinoid receptor activation in the juvenile rat brain results in rapid biomechanical alterations: Neurovascular mechanism as a putative confounding factor. *J Cereb Blood Flow Metab*. 2016;36(5):954-964. doi:10.1177/0271678X15606923.

47. Freimann FB, Müller S, Streitberger K-J, Guo J, Rot S, Ghori A, Vajkoczy P, Reiter R, Sack I, Braun J. MR elastography in a murine stroke model reveals correlation of macroscopic viscoelastic properties of the brain with neuronal density. *NMR Biomed*. 2013;26(11):1534-1539. doi:10.1002/nbm.2987.

48. Millward JM, Guo J, Berndt D, Braun J, Sack I, Infante-Duarte C. Tissue structure and inflammatory processes shape viscoelastic properties of the mouse brain. *NMR Biomed*. 2015;28(7):831-839. doi:10.1002/nbm.3319.

49. Gerischer LM, Fehlner A, Köbe T, Braun J, Sack I, Agnes F. High resolution MR elastography of the hippocampus as a novel biomarker for Alzheimer's disease? *Clinical Neurophysiology*. 2016;127(9):e216-e217. doi:10.1016/j.clinph.2016.05.029.

50. Schwarb H, Johnson CL, McGarry MDJ, Cohen NJ. Medial temporal lobe viscoelasticity and relational memory performance. *NeuroImage*. 2016;132:534-541. doi:10.1016/j.neuroimage.2016.02.059.

51. Mahieu-Williame L, Gaillard S, Grenier D, Bolbos R, Langlois JB, Lamberton F, Camarasu-Pop S, Beuf O. *SNR and Volume Characterization of RF Coils: A Simple Procedure and an Automatic Post-Processing Tool for a Straightforward Comparison.* 2017. https://hal.archives-ouvertes.fr/hal-01693554. Accessed March 14, 2019.

52. Glatard T, Lartizien C, Gibaud B, Ferreira da Silva R, Forestier G, Cervenansky F, Alessandrini M, Benoit-Cattin H, Bernard O, Camarasu-Pop S, Cerezo N, Clarysse P, Gaignard A, Hugonnard P, Liebgott H, Marache S, Marion A, Montagnat J, Tabary J, Friboulet D. A Virtual Imaging Platform for Multi-Modality Medical Image Simulation. *IEEE Transactions on Medical Imaging*. 2013;32(1):110-118. doi:10.1109/TMI.2012.2220154

Table 1: MR acquisition parameters. MRE acquisitions were repeated 3 times at each frequency, with MEGs in slice, phase and read directions (NA, not available).

	MSME	MR elastography					
Field of view	25 x 25 mm²	25 x 25 mm²					
Matrix	128 x 128	64 x 64					
Spatial resolution	195 x 195 µm²	391 x 391 µm²					
Slice thickness	1 mm	1 mm					
Number of slices	7	7					
Number of phase offset images	NA	8					
Mechanical excitation frequency (Hz)	NA	400	600	800	900	1000	1200
Number of MEG periods	NA	1	2	8	9	10	8
Echo time (ms)	12 – 24 – 36 – 48 – 60 – 72	15	15	28	30	28	21
Repetition time (ms)	5033	1200	1000				
Acquisition time	8’3”	5’3”	4’16”				

Figures

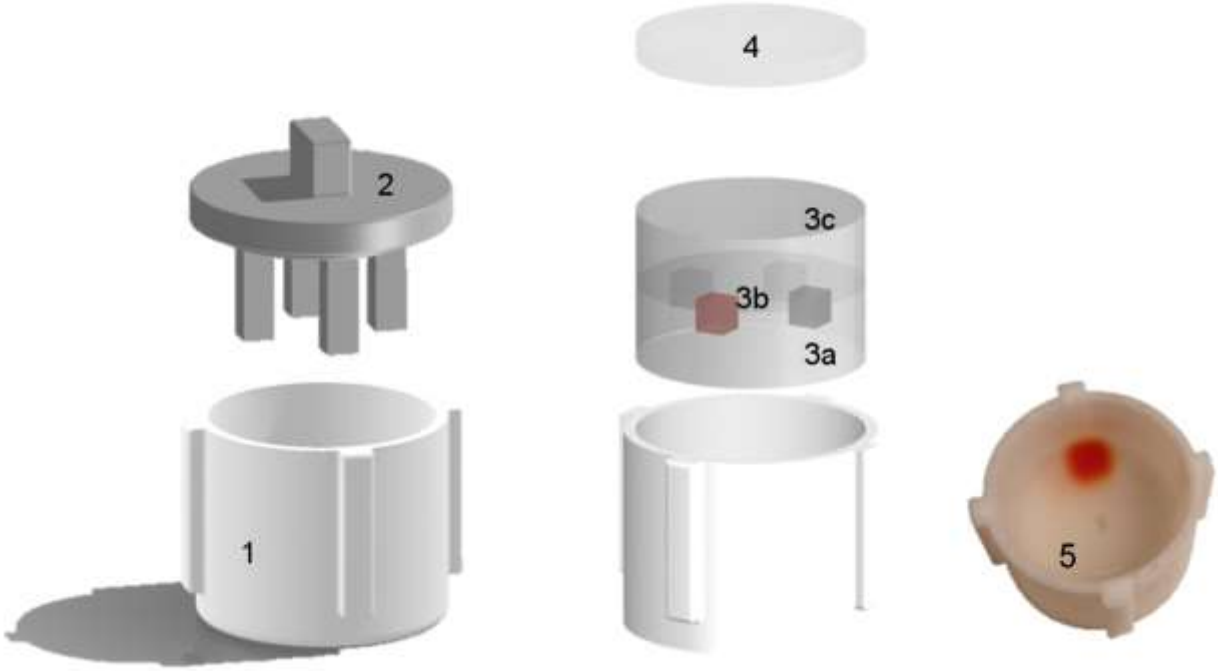

Figure 1: Schematic view of 1) the sample holder and 2) the mold used to create inclusions. The different layers of the phantom are represented: 3a) 1% agarose. The mold put on the sample holder was used to create the 4 imprints in which 3b) inclusions were created, containing 1.35% agarose and BSA or fibril solutions. After cooling, 3c) a third layer of 1% agarose was added. Lastly, 4) a thin layer of paraffin adhering to the edges of the sample holder was poured. 5) A photograph of the phantom in its holder.

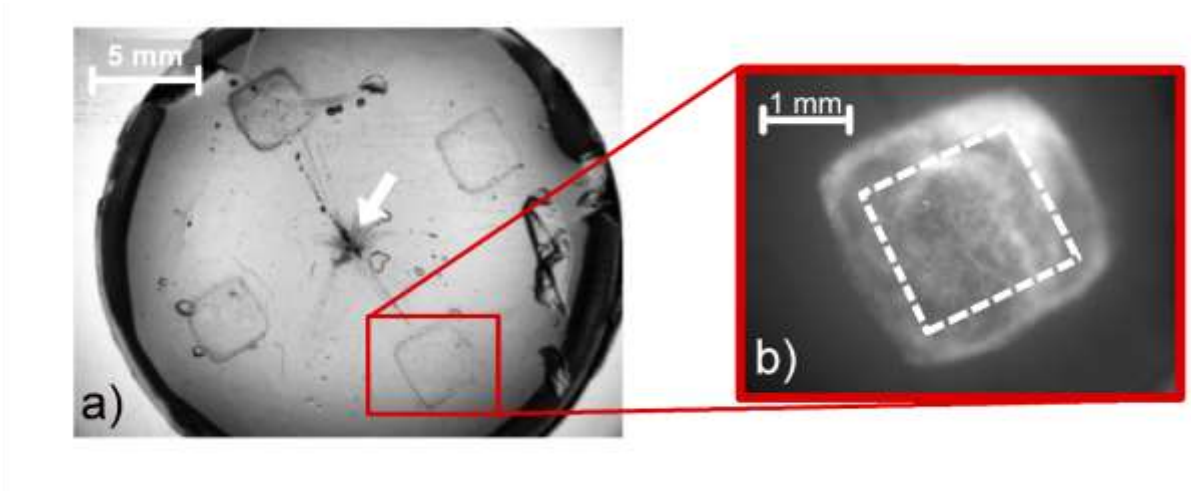

Figure 2: a) Bright field image of a phantom with a 1x magnification. A needle (presented in Figure 3) mark is shown by a white arrow. b) Macrofluorescence image of an α-Syn inclusion with a 5X magnification. Green fluorescence, appearing here in white, indicates binding of thioflavin-T to fibrils. In this inclusion, the edges of the inclusion are clearly visible, indicating that no leakage of fibrils has happened. An ROI is drawn, avoiding the edges of the inclusion (white dashed square).

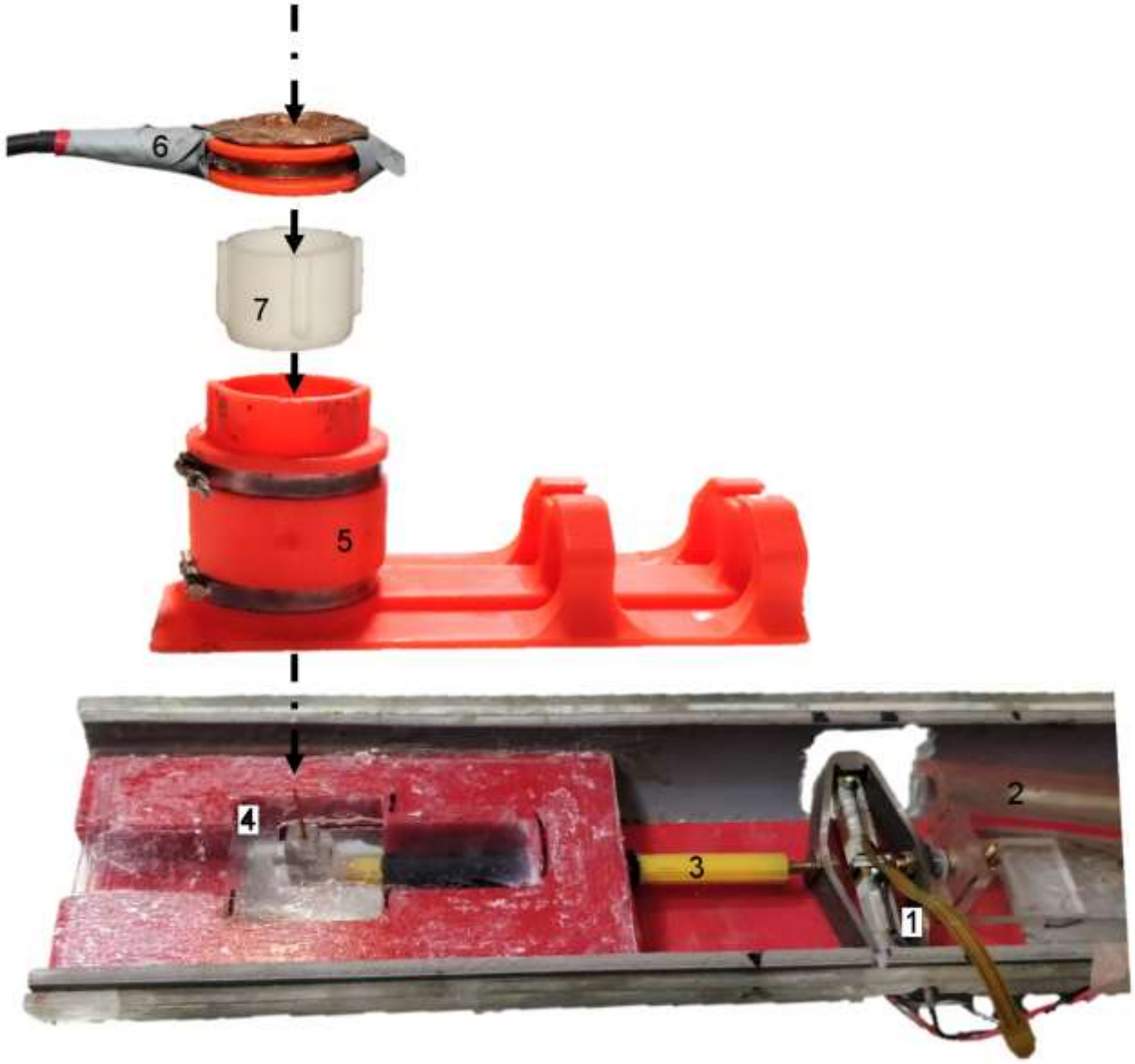

Figure 3: Elastography bench dedicated to small samples: 1) a piezoelectric driver for wave generation (APA100M Cedrat Technologies), cooled by 2) an air intake; 3) a star-shaped rod transmitted movement to 4) a cactus needle, in direct contact with the sample; 5) a 36 mm diameter Helmholtz coil and 6) associated coupling loop used for signal acquisition and transmission. 7) The sample holder was slid inside the coil.

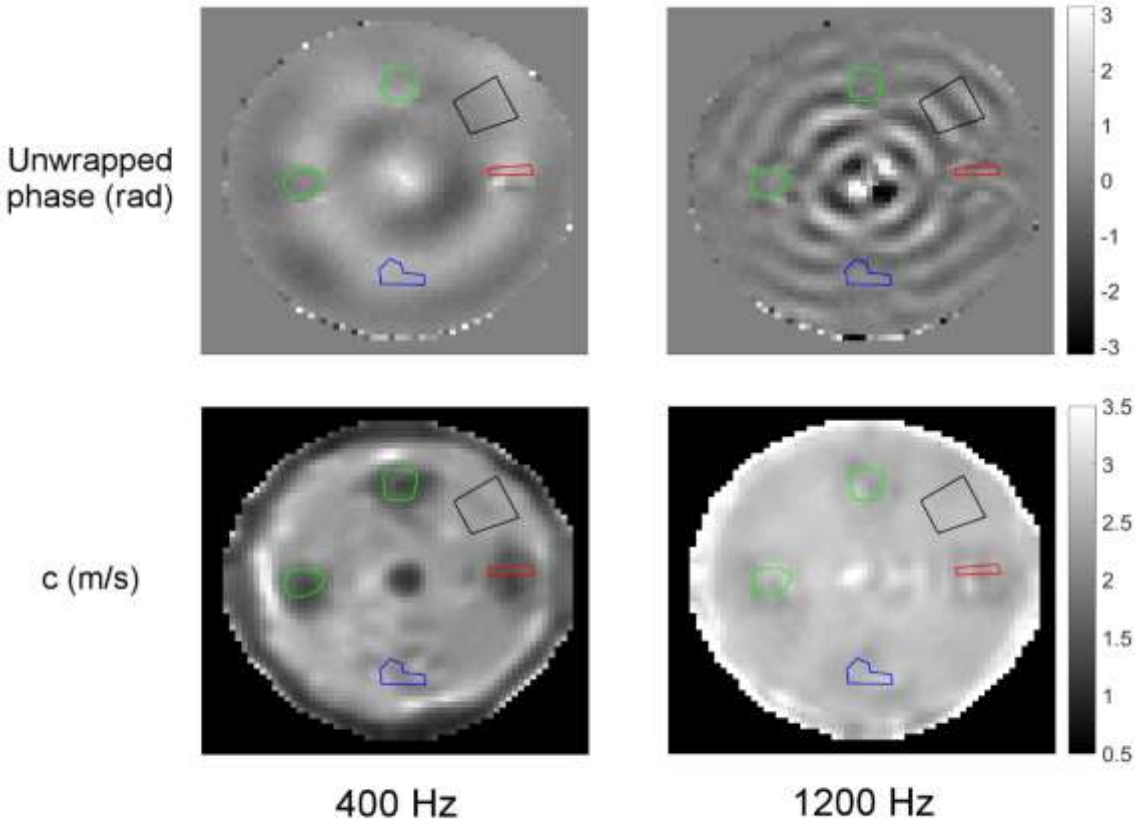

Figure 4: MRE unwrapped phase and wave speed obtained at 400 and 1,200 Hz (motion encoding direction orthogonal to the slice). Aβ, α-Syn and BSA inclusions and agarose ROIs are represented in green, red, blue and black, respectively.

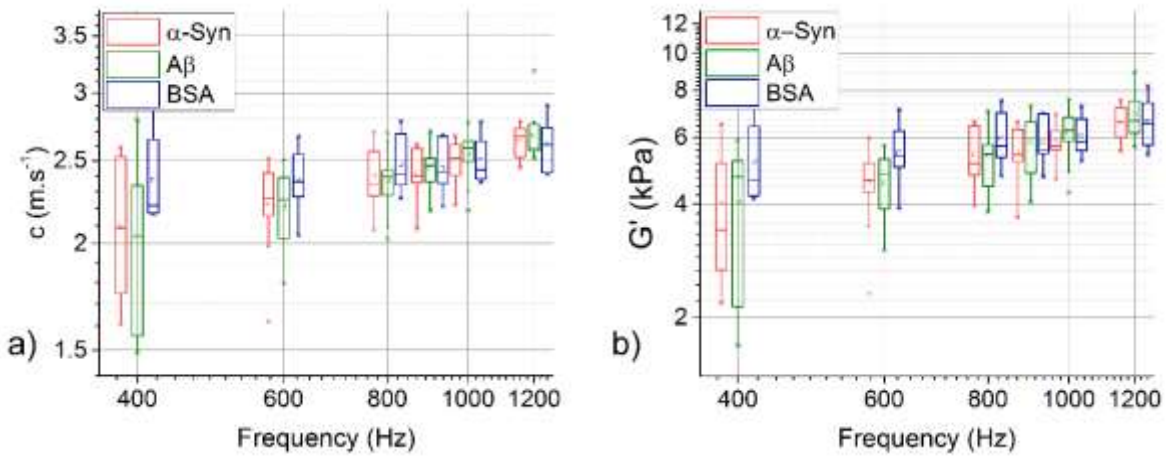

Figure 5: Boxplots of a) wave speed c and b) storage modulus G' computed from ROI included in inclusions containing α-Syn, Aβ fibrils and BSA for frequencies varying between 400 and 1,200 Hz. For each frequency, 11, 10 and 7 values are represented for α-Syn, Aβ40 and BSA, respectively. Each box of the plot contains values from the 25th to the 75th percentile. Maximum and minimum values are symbolized by crosses, mean value by a square and median by a line in the box.

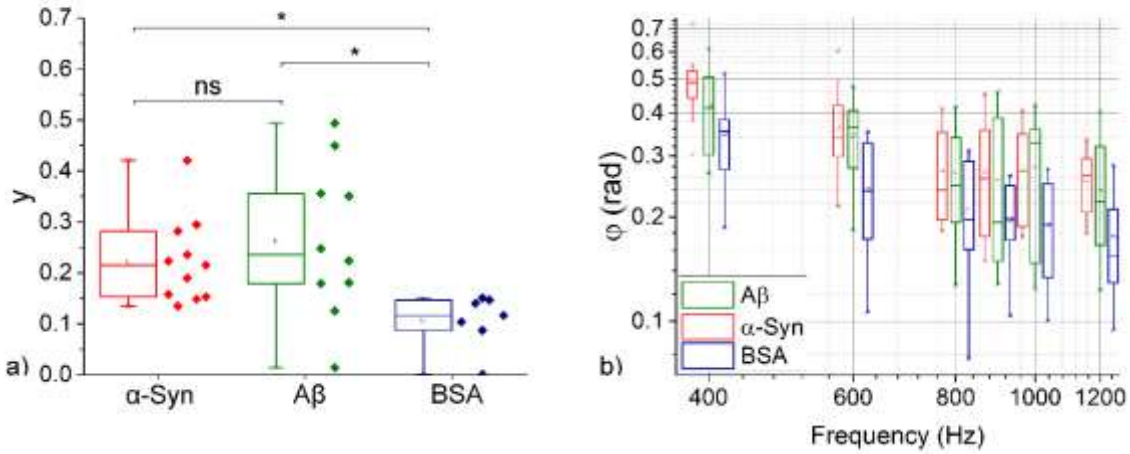

Figure 6: a) Boxplots of exponent y for α-Syn, Aβ and BSA. 11, 10 and 7 values are represented as dots for α-Syn, Aβ and BSA, respectively. b) Boxplots of phase angle φ for α-Syn, Aβ and BSA inclusions (11, 10 and 7 values for each box plot, for α-Syn, Aβ and BSA, respectively). Each box of the plot contains values from the 25th to the 75th percentile. Maximum and minimum values are symbolized by crosses, mean value by a square and median by a line in the box.

Supplementary materials

1. Comparison of a volume coil and a handmade Helmholtz coil

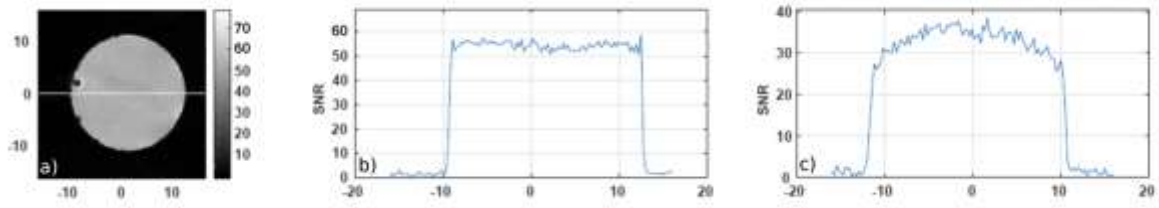

Figure S1: a) Image of a 20x20x20 mm^3 $NiSO_4$ sample made with a 32 mm diameter volume coil in quadrature (Bruker, Ettlingen, Germany). A white line shows the direction in which the b) associated SNR profile has been made. c) Profile made in the same direction with the handmade Helmholtz coil used in this study. SNR was 50 ± 1 in the 32 mm coil, i.e. about 50/√2 ≈ 35 ± 1 without quadrature detection, and 32 ± 1 in the Helmholtz coil. Results were obtained using the MRI characterization tool[51] (https://vip.creatis.insa-lyon.fr/documentation/mri_charact.html) which is available online through the Virtual Imaging Platform[52] (https://vip.creatis.insa-lyon.fr/).

2. BSA and agarose

Variable	Frequency range	Agarose	BSA
G'	400-1200 Hz	5.7 ± 0.8 – 6.7 ± 0.6 kPa	5.2 ± 1.4 – 6.6 ± 1.0 kPa
c	400-1200 Hz	2.3 ± 0.1 – 2.6 ± 0.1 $m.s^{-1}$	2.4 ± 0.3 – 2.6 ± 0.2 $m.s^{-1}$
φ	400-1200 Hz	0.09 ± 0.02 – 0.20 ± 0.05 rad	0.17 ± 0.06 – 0.35 ± 0.10 rad
y	/	0.12 ± 0.02	0.11 ± 0.05

Table S2: Range of mean ± standard deviation obtained for G', c and φ for all investigated frequencies and for y in the agarose ROI, far from all inclusions and in the BSA inclusion, used as control for the evaluation of a fibril effect.

3. Transmission electronic microscopy of α-Syn and Aβ fibrils

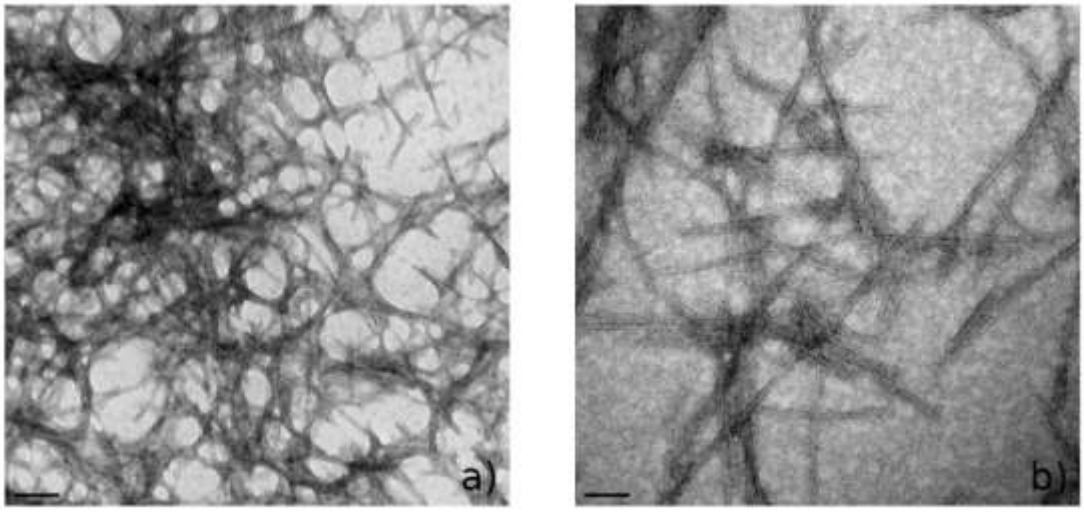

Figure S3: Transmission electronic microscopy of a) α-Syn and b) Aβ fibrils. Scale at the right corner corresponds to 100 nm.